Surfaces and Interfaces 48 (2024) 104314

Contents lists available at ScienceDirect

Surfaces and Interfaces

journal homepage: www.sciencedirect.com/journal/surfaces-and-interfaces

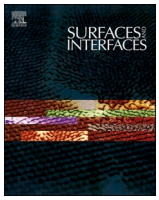

Nanoscale hydrate adhesion on organic surfaces

Rui Ma, Senbo Xiao *, Yuanhao Chang, Jianying He, Zhiliang Zhang *

NTNU Nanomechanical Lab, Department of Structural Engineering, Norwegian University of Science and Technology (NTNU), Trondheim 7491, Norway

ARTICLE INFO

Keywords:
Gas hydrate
Adhesion
Organic monolayers
Cohesive failure
Adhesive failure

ABSTRACT

The future of addressing persistent gas hydrate blockages in oil and gas pipelines lies in the realm of surface material design, aimed at reducing environmental harm and energy inefficiencies associated with traditional chemical additives or heat-based approaches. A comprehensive understanding of hydrate-surface interactions is crucial for effective material-based solutions. Our study examined gas hydrate adhesion on diverse organic monolayer surfaces, utilizing Molecular Dynamics (MD) simulations to explore the impact of surface flexibility, gas concentration, and crack locations on hydrate adhesion strength. Results highlight the dependence of adhesion strength on surface functional groups. Hydrophobic interfaces are susceptible to weakening through a "gas coating", while hydrophilic groups, like hydroxyl, strengthen adhesion through hydrogen bonding, altering the fracture behavior from adhesive failure to cohesive failure. Unexpectedly, the flexibility of monolayers has minimal influence, especially on hydrophobic surfaces. Tensile testing identified six distinct fracture interfaces, with the ice-hydrate interface displaying the highest adhesion strength, highlighting the detrimental impact of hydrogen bonding on interface weakening. These findings significantly deepen the understanding of soft surface properties influencing gas hydrate adhesion, offering a valuable guide for designing and fabricating highly efficient flexible anti-hydrate surfaces.

1. Introduction

Gas hydrate deposition and subsequent plugging present a significant threat to the oil and gas industry, particularly in deep-water resource exploration and transportation [1–7]. These ice-like substances, resulting from the union of water and small gas molecules, can form within pipelines operating under low-temperature, high-pressure conditions [8–10]. Uncontrolled growth of these hydrate masses on the inner walls of pipelines substantially reduces the pipeline's diameter, obstructs fluid flow, and endangers infrastructure integrity, thus imperiling the safety and efficiency of oil and gas production [3,11,12]. To address these challenges, extensive research efforts have been dedicated to developing prevention and mitigation strategies, ensuring the safe and efficient operation of petroleum and natural gas extraction and transportation.

Current approaches for managing natural gas hydrates primarily rely on chemical additives or active heating methods, which often prove to be expensive, energy-intensive, and environmentally detrimental [13–19]. In recent years, the focus has shifted toward exploring innovative strategies rooted in the surface engineering of materials [20–25]. The concept of designing surfaces to repel or mitigate the adhesion of gas hydrates holds significant promise for more effective and environmentally sustainable strategies. This approach usually harnesses specific surface properties of materials, such as low surface energy and structural hydrophobicity, akin to materials used in anti-icing applications [26–30].

Anti-icing surfaces typically have such properties: repel incoming water droplets, inhibit ice nucleation, and substantially reduce ice adhesion strength [27]. The resistance of these surfaces to water suggests that similar strategies can be adapted for anti-hydrate applications. For instance, inspired by the micro-porous structure beneath the smooth exterior of an onion, researchers have designed surfaces with hydrate adhesion strength as low as 2.9 kPa [31]. Additionally, fracture mechanics designs based on multiscale crack initiation mechanisms at the interface offer another avenue for research in the anti-icing field [27]. Moreover, the use of materials with low interfacial toughness can expand the scope of de-icing to large scales [32]. Given the similarities between hydrates and ice, the strategies of lowering adhesion by promoting interface cracking hold promise for anti-hydrate surface design.

Promoting crack initiation and propagation can significantly reduce interfacial adhesion [33,34]. Surface morphology and multiscale hierarchical assembly structures on solid surfaces often trigger crack initiation at the interface [35,36]. Incomplete contact between hydrate/ice

* Corresponding authors.
E-mail addresses: senbo.xiao@ntnu.no (S. Xiao), zhiliang.zhang@ntnu.no (Z. Zhang).

https://doi.org/10.1016/j.surfin.2024.104314
Received 24 January 2024; Received in revised form 14 March 2024; Accepted 7 April 2024
Available online 8 April 2024

and the substrate surface, including micro-pores where water cannot penetrate or gaps filled with gas in the so-called "Cassie" state, can also serve as crack initiation sites, significantly reducing interfacial strength [37–39]. Especially for some soft materials, stress concentration locations generated by deformation during the freezing process due to the mismatch between hydrate/ice and the surface can become favorable sites for triggering crack initiation [40–42]. Unlike numerous studies carried out on the adhesion of hydrates to hard surfaces, there is limited exploration of flexible surfaces in this field, and the specific features of these surfaces controlling interfacial strength remain undetermined.

In contrast to rigid mineral or metal surfaces, flexible surfaces are characterized by higher deformability and a greater variety of functional groups [43,44]. The deformability or flexibility of the surface frequently facilitates interface matching, yet the structure and degree of matching depend on the type of functional groups present [45]. Studies indicate that hydroxyl groups exposed to water on organic surfaces can arrange themselves into structures like ice [43,46,47], but whether this increased matching affects adhesion strength remains unclear. A comprehensive understanding of the adhesion behavior of hydrates on flexible surfaces can complement the interaction mechanisms between hydrates and different types of surfaces, which is critical for the development of flexible anti-hydrate surfaces, such as coatings.

This study aims to investigate the adhesion behavior of gas hydrates on flexible surfaces, including surface fluctuations and the influence of different functional groups, through molecular dynamics simulation methods. Our focus will be on typical flexible monolayers as the objects of study. These monolayers exhibit a well-defined structure, akin to the disk flower, while maintaining a level of flexibility that distinguishes them from rigid solids (treating the surface as rigid body). This choice enables our research to attain a controlled shift from solid to flexible surfaces, a critical step in our effort to study hydrate adhesion on varied materials. By simulating the interaction processes and adhesion behavior of hydrates on monolayers, we aim to unveil the adhesion mechanisms of hydrates on flexible surfaces, offer new insights into the interaction behavior between gas hydrates and surfaces, and provide a scientific foundation for the development of innovative passive anti-hydrate surface.

2. Modeling and methods

2.1. Model systems for gas hydrate adhesion on monolayers

A sandwich model system is used to simulate and analyze the adhesion processes of gas hydrates on monolayers, as depicted in Fig. 1. The general system configuration comprises a pre-built hydrate crystal as the top layer, organic monolayers as the bottom layer, and an intermediate layer (IML) in between. The design of this sandwich model aims to faithfully replicate the evolution of transitional structures between gas hydrates and monolayers, making the spontaneous formation of rational interface structures based on interfacial composition and environmental conditions. In this study, the top layer consists of the standard sI hydrate structure, composed of a 4 × 4 × 3-unit cell (2208 water molecules and 384 gas molecules), capturing the atomic characteristics of hydrate particles. The bottom organic monolayers consist of linear n-alkane or alcohol molecules (C_n or $C_{n-1}OH$) arranged in a simple cubic lattice structure, wherein the surface's wetting properties are regulated through the functional groups on the monomer tail chains. Specifically, $-CH_3$ and -OH groups were chosen for hydrophobic and hydrophilic organic monolayers, respectively. A lattice constant of 4.3 Å was deliberately chosen to ensure that the area per monomer and the tilt of the carbon chain closely matched experimental values [43,48]. All monolayer models have the same surface area, approximately 51.6 Å × 51.6 Å. The region between hydrates and monolayers is filled with an amorphous water layer containing four different concentrations (0 %, 50 %, 100 %, and 200 %) of gas molecules, serving as the pre-built IML. Models whose water-gas ratios are the same as sI standard hydrates are denoted as 100 %. Four IMLs with different gas concentrations encompass diverse scenarios from pure water to gas oversaturation. We performed dynamic simulations on all systems containing distinct sets of IML and gathered all the data for analysis and comparison. In the simulation system, all boxes feature periodic boundary conditions and vacuum buffers to isolate atomic interactions between the hydrate top and monolayers.

2.2. Force fields and atomistic parameters

The interactions among water molecules are modeled by a single-point mW model, incorporating the three-body Stillinger-Weber (SW) potential to account for angle-dependent atomic interactions [49,50]. This model accurately captures the tetrahedral structure of hydrogen-bond networks, a critical aspect in the study of ice and hydrates [51–56]. Gas molecules, such as methane within hydrates, are described using the "M" particle model, a common choice for simulating small guest molecules [51,52]. "M" particles interact with mW water molecules using a two-body SW potential. The alkane/alcohol monomers are modeled at the united-atom level, where the CH_3 and CH_2 groups are simulated using the Leonard-Jones interaction of OPLS-UA force field [57]. All sites in monomer share identical bonded parameters [43,58]. Interactions between OPLS carbon types and mW hydroxyl groups are depicted using Lennard-Jones potentials, with $\varepsilon_{hc} = 0.118$ kcal mol^{-1} and $\sigma_{hc} = 3.905$ Å, resembling CH_2-CH_2 interactions in OPLS-UA. Interactions between OPLS carbon types and mW water are described through the Leonard-Jones potential with $\varepsilon_{wc} = 0.17$ kcal mol^{-1} and $\sigma_{wc} = 3.536$ Å [43,58]. The interactions between hydroxyl

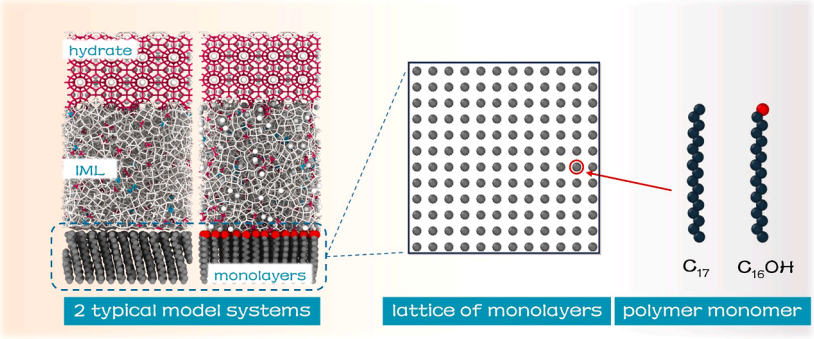

Fig. 1. Schematic of the simulation model systems. Hydrophobic and hydrophilic organic monolayers are formed by C_{17} and $C_{16}OH$ molecules, arranged in a simple cubic lattice. The carbon chains and hydroxyl groups in the monomer are represented as dark gray and red beads, respectively. Pre-built hydrates and amorphous water molecules are depicted by pink and white bonds, respectively. Gas molecules are rendered as small white balls. The color scheme applies to all snapshots in the following figures.

and water are the same to those among water molecules.

2.3. Simulation settings of gas hydrate adhesion–solidification on monolayers

The LAMMPS software (Large-scale Atomic/Molecular Massively Parallel Simulator) was employed for this simulation study [59]. The initial atomic structure underwent energy minimization, followed by 1 ns equilibration at 270 K to allow for the structural relaxation of the initial IML. During this stage, the pre-built hydrate layer remained fixed to prepare the stable initial simulation system for subsequent IML solidification processes. The pre-equilibrated system was then quenched to 210 K within an NVT ensemble for a dynamic simulation lasting 200 ns. This duration proved adequate for the IML to adopt stable solidified configurations. Temperature control was achieved using a Nose-Hoover thermostat with a coupling constant of 0.1 ps [60,61]. A time step of 5 fs was employed in the simulations [43], with each system consisting of 5 independent runs to ensure the statistical significance of the IML solidification process. Throughout the simulation, system properties were continually monitored and recorded. Final system configurations were collected and used for the tensile testing. Snapshots of simulation system are rendered through the visualization software Ovito [62].

2.4. Tensile test of hydrate adhesion

To investigate the adhesion strength of hydrates binding to organic monolayers through IML, tensile tests were conducted on the pre-built hydrate layer within the system, following a methodology consistent with previous studies [21,23,63]. A force constant of 1 kcal/mol/Å^2 was applied to the centre of mass of the pre-built hydrates using a moving harmonic spring, set to retract from the monolayers at a constant speed of 0.0001 Å/fs. This allowed the stretching harmonic spring to exert tension on the hydrates, leading to their separation from the substrate. The force distribution of the harmonic spring was continuously monitored, with tension steadily increasing until a sudden drop signified the rupture of hydrates from the base surface. All tensile tests were terminated upon hydrate separation. The adhesion strength of hydrates was determined by recording the highest tensile force and normalizing it according to the surface area of monolayers. A consistent stretching velocity was maintained across all tests to ensure comparability in assessing differences in adhesive strength.

3. Results and discussions

3.1. IML adhesion-solidification process on monolayers

Upon the attachment of hydrate nuclei to the surface, further solidification significantly enhances their adhesion strength. Typically, the solidification of intermediate layer (IML) structures is predominantly temperature-driven. However, the gas content and distribution, surface type and functional group also exert a substantial influence on solidification efficiency and structure. The ultimate solidified IML structure plays a crucial role in determining its adhesion strength on the surface, aligning with the general principles governing hydrate adhesion on solid surfaces [21,23,64,65].

3.1.1. Two typical solidification modes

In this study, the CHILL+ algorithm [66] is employed to characterize evolution in system structure. CHILL+ uses the count of staggered and eclipsed water-water bonds to distinguish different ice, and hydrates. These water structures contain varying numbers of staggered and eclipsed bonds. The methodology employs the number of water molecules to represent variations in structure size, a common approach in molecular modeling studies related to hydrates, ice [55,67], as depicted in Fig. 2. An increase in the number of water molecules identified as crystals signifies the growth of crystalline.

Here, the monolayer formed by the arrangement of C_{17} is selected as representative example of flexible hydrophobic surfaces to investigate hydrate adhesion behavior. We summarize all simulation trajectories, encompassing four different gas concentrations, and deduce two typical modes of the IML solidification process, referred to as *Hydrate/Ice Competition* (HIC) and *Hydrate Induced Growth* (HIG). Both modes share a common starting point, commencing with top-down growth of hydrates from high-temperature quenched simulations. At this stage, induction growth initiated by pre-built hydrate crystals predominates, as illustrated in the snapshots in Fig. 2a and c. However, this induction growth process may be disrupted by the ice nucleation. Prior to the complete transformation of initial IML into hydrates, if stable ice nuclei form within the amorphous regions, ice usually competes with the established hydrate lattice, as indicated by the growth curve in Fig. 2b, which

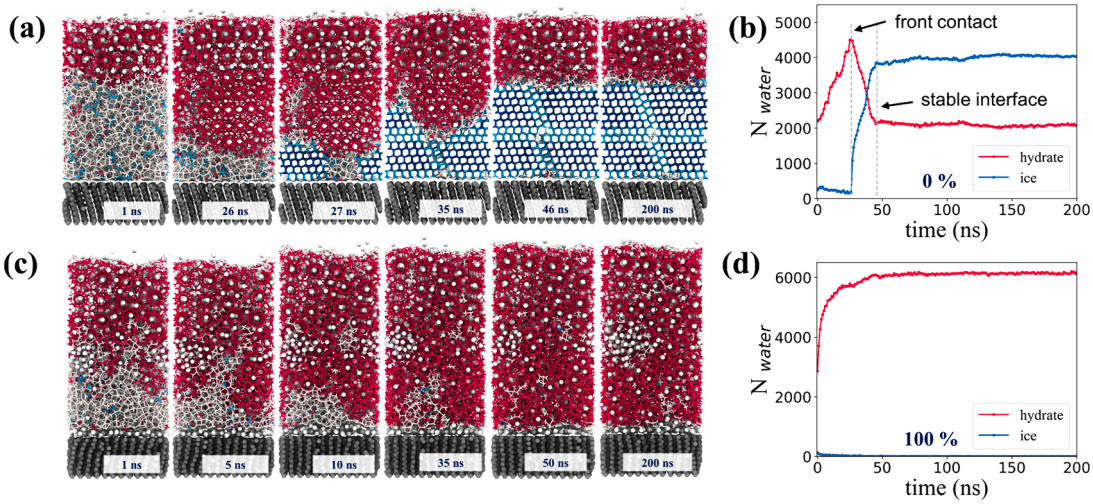

Fig. 2. Two typical modes in hydrate adhesion-solidification process on flexible monolayers. (a) and (b) depict dynamic snapshots with timestamps under the *Hydrate/Ice Competition* (HIC) mode and growth curves of hydrates and ice during the adhesion-solidification process, separately. (c) and (d) show the same content but under the *Hydrate Induced Growth* (HIG) mode. The percentages in (b) and (d) represent the initial IML gas content. A gas concentration of 0 % indicates that there are no gas molecules present in IML included in the model. A gas concentration of 100 % indicates that the gas-water ratio in the IML included in the model aligns with standard sI hydrates. The number of water molecules in the ice or hydrate structure represents its size. Light and dark blue sticks are used to distinguish cubic and hexagonal ice identified by the CHILL+ algorithm, and this color scheme applies to all subsequent images.

comprehensively delineates the competitive process illustrated in Fig. 2a. Hence, in the IML solidification process, the roles of the upper and lower layers are distinct. Hydrate growth is predominantly governed by the pre-built hydrate layer, whereas the heterogeneous nucleation of ice is mainly influenced by the solid surface.

It is noteworthy that, during the competition growth of ice and hydrates, the hydrate structures that are replaced by ice are often empty, as depicted in Fig. 2a. It is important to emphasize that while empty cages are included in real hydrate structures, their stability is typically limited [68]. Elevated pressure conditions often result in the collapse of numerous continuous empty cage structures [23]. This phenomenon reflects a state of thermodynamic metastability of empty cages, also elucidating the propensity for ice to displace such empty cage structures. The ice nuclei generated within IML only stop to grow once they almost replace all newly formed empty cages, maintaining an equilibrium with the pre-existing hydrate crystals, as depicted in Fig. 2b. This phenomenon reflects the higher thermodynamic stability of ice relative to empty hydrate structures at lower temperatures, with the presence of gas molecules contributing to the stability of hydrate cages. An almost identical phenomenon is also observed during the solidification of hydrate adhesion on solid surfaces [21,23]. Thus, the polymorphic phenomenon of water structure often leads to the complexity of the final stable structure at the hydrate-substrate interface.

3.1.2. Role of gas molecules in the IML solidification process

By comparing simulation results from systems with varying gas concentrations, we have observed that ice nucleation occurs exclusively in configurations with a gas molecule content of 0 %, as illustrated in Fig. 3a. This phenomenon suggests that the presence of gas molecules at a certain concentration within IML effectively disrupts or delays ice nucleation. Parallel simulations for each configuration reveal the presence of two types of solidified IML structures: ice or empty hydrate cages in pure water IML (labeled as 0 %), explaining the significant fluctuations in the blue curve in Fig. 3b. As the concentration of gas molecules increases, IML displays a faster rate of hydrate growth, as depicted in the hydrate growth curve in Fig. 3b. Hence, gas molecules in the IML solidification process typically have a dual role, inhibiting ice nucleation while accelerating the growth of hydrates. Furthermore, newly formed hydrate structures in gas-bearing IML often exhibit greater disorder compared to the single crystals formed in pure water IML, resembling a hydrate mixture, as illustrated in Fig. 3d.

As the gas content in the IML gradually increases, phase separation emerges within the system configurations, typically manifested as the initial IML gas exsolution during the equilibration process, as depicted in Fig. 3a. Since the selected monolayer comprises C_{17} molecules, the hydrophobic alkyl (-CH_3) groups are exposed within the initial IML. Due to the stronger cohesive interactions between water molecules, oversaturated gas within the initial IML can exsolve at the IML/monolayer interface. Furthermore, with a further increase in gas molecule content within the system, oversaturated gas can also nucleate in the form of bubbles within the IML. Subsequently, during the solidification process, these generated bubbles are trapped within the sintered IML. The density curves of gas molecules from a set of systems with different gas concentrations, as shown in Fig. 3c, depict the distribution of gas molecules within the system. The phenomenon of interfacial gas cushions and internal bubbles aligns with previous findings [23,69,70], and such heterogeneous structures are considered a form of micro-crack initiator (MICI) [27], which can significantly reduce the adhesion strength of hydrates on substrates in certain scenarios.

3.2. Impact of surface flexibility on solidified IML structures

To further assess the potential influence of the flexibility of organic monolayers on the solidified IML structures, we introduced a control group with a constrained monolayer. Specifically, in this control group simulation, we fixed every C_{17} molecule as a rigid body at the beginning, resulting in a rigid surface with the same lattice constant and arrangement. All intermolecular interaction parameters remained unchanged in order to observe the potential effects on the interface structure during the transition from rigidity to flexibility. The CHILL+ algorithm was still

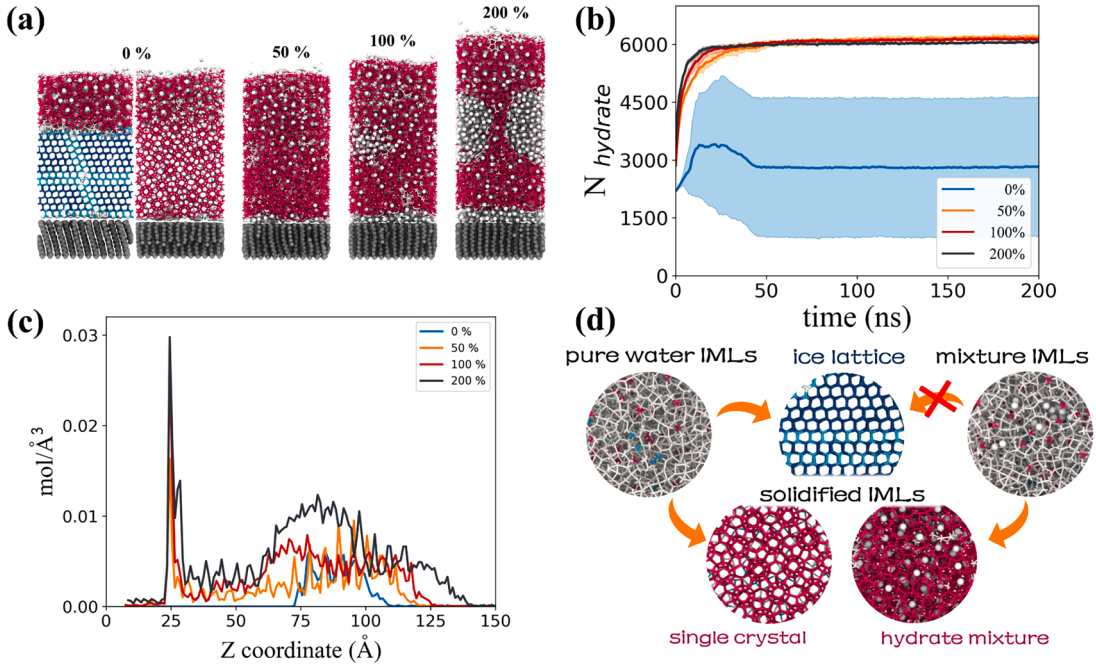

Fig. 3. The effect of gas molecules on the IML adhesion-solidification process. (a) The final solidification configurations of the IML under different gas contents. The presence of gas molecules inhibits ice nucleation. (b) Growth curves of hydrates during the solidification process of IML with varying gas contents. Higher gas concentrations accelerate hydrate growth. (c) Gas density distribution curves along the substrate normal direction after solidification of IML with varying gas contents. (d) Schematic representations of solidified structures for IML with different gas contents. Pure water IML can solidify into ice or hydrate single crystal. Gas-containing IML tends to form hydrates, with the structure influenced by gas content and distribution, often resulting in a hydrate mixture.

employed to monitor the solidification process of IML. As expected, the same "HIC" and "HIG" modes were observed on the rigid monolayer, as depicted in Fig. 4. The process follows an entirely consistent pattern except for the ice nucleation time. It emphasizes that the primary structure of solidified IML is predominantly regulated by temperature and the concentration of enclosed gas molecules.

While the primary structure of solidified IML remains largely unaffected by the substrate, the structure and composition of the IML/substrate interface layer are strongly influenced, as illustrated in Fig. 5. The most notable characteristic of a rigid surface, compared to a flexible one, is its inability to deform. Consequently, the adjacent layers on the rigid surface must make certain structural "sacrifices" to partially deform and compensate for the mismatch with the solid surface lattice. In contrast, a flexible surface can better match the lattice of water through the deformation of itself. This phenomenon is more pronounced in structures formed by water molecules (Fig. 5a, 0 %), as oriented hydrogen bonds exist between water molecules. However, because C_{17} is inherently more hydrophobic, the impact of this interfacial lattice mismatch on water molecule density remains relatively limited, as reflected in the radial distribution function (RDF) of the substrate-interfacial water (Fig. 5b).

For gas molecules, weaker van der Waals interactions are insufficient to constrain them into forming a "collective layer" as observed in water. In this scenario, the arrangement of the substrate surface significantly influences the position of each nearly independent gas molecule distribution. Consequently, gas molecules on the more symmetric rigid monolayer form more ordered, layered distributions. Conversely, near the flexible monolayer, owing to the deformability of monomer C_{17}, gas molecules together with surface monomer form more complex, chaotic structures, as evident in the broader and smoother set of shapes displayed in the RDF in Fig. 5c. The flexibility of the surface generates a more disordered interface.

3.3. Role of hydrophilic functional groups on monolayer in hydrate adhesion

In addition to flexibility, organic monolayers are characterized by a rich variety of functional groups. Given that surfaces formed by C_{17} exhibit hydrophobic properties, in this section of the study, we explore the influence of hydroxylation modification of the monolayer on wettability – an important parameter determining hydrate adhesion strength. Hydroxylation modification of the monolayers is achieved by replacing the methyl group ($-CH_3$) at the end of each C_{17} with a hydroxyl group (-OH) represented by mW water molecules. The hydroxylated monolayer exhibits good hydrophilicity, whatever on rigid and flexible substrates, as depicted in Fig. 6. Hydroxylated monolayers consistently lead to the presence of a water layer near the surface. The dense adsorption of water molecules at the interface also results in a significant reduction of gas concentration in that region. Hence, ice structures can typically be observed in proximity to the hydroxylated monolayers, as shown in Fig. 6a.

The flexibility of C_{16}-OH molecules on monolayer significantly reduces the mismatch between the ice and substrate, as illustrated in Fig. 6b. The rigid hydroxylated monolayer consistently leads to the formation of non-hexagonal water crystal lattices, where the first layer of water molecules acts as a transitional structure with subsequently generated ice lattice. However, the situation differs on flexible surfaces. The fluctuation of C_{16}-OH monomer enables them to actively deform while interacting with water molecules, compensating for the mismatch between the substrate and ice lattice. Same as flexible C_{17} monolayer, flexible C_{16}-OH monolayer also achieves the transition in structure through their fluctuation and deformation, enabling the first-layer water molecules to form more hexagonal ice lattices. The RDF of water molecules on rigid and flexible hydroxylated monolayers clearly reflect the impact on adjacent water structures, as shown in Fig. 6c. Flexible hydroxylated monolayer promote the formation of well-bedded structures among interface water molecules, while rigid surfaces result in a looser adjacent water layer, manifested as broader peaks in the RDF.

3.4. Tensile test for hydrate adhesion strength on monolayers

All stable solidified configurations from systems involving rigid hydrophobic, rigid hydrophilic, flexible hydrophobic, and flexible hydrophilic monolayers, as described in the previous sections, were collected for tensile tests to determine adhesion strength. Adhesion strength was obtained by applying a spring force to separate the hydrate from monolayers, as depicted in Fig. 7a. Detailed settings for the tensile test can be found in Section 2.4. The maximum spring force measured when structural rupture was normalized by the cross-section of these monolayers to adhesion strength. Fig. 7b and c categorize the measured adhesion strengths in different systems based on hydrophobic ($-CH_3$) and hydrophilic (-OH) monolayers, with flexible and rigid surfaces

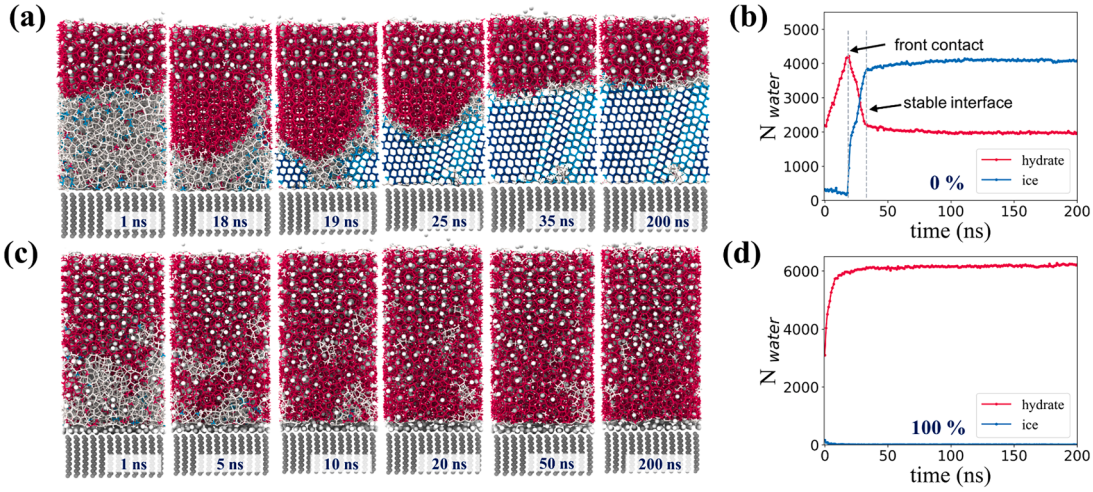

Fig. 4. Two typical modes in hydrate adhesion-solidification process are also identified on the rigid monolayers. (a) and (b) depict dynamic snapshots with timestamps under the "HIC" mode and growth curves of hydrates and ice during the adhesion-solidification process, separately. (c) and (d) show the same content but under the "HIG" mode. The percentages in (b) and (d) represent the initial IML gas content in this case. A gas concentration of 0 % indicates that there are no gas molecules present in IML included in the model. A gas concentration of 100 % indicates that the gas-water ratio in the IML included in the model aligns with standard sI hydrates. The number of water molecules in the structure represents its size.

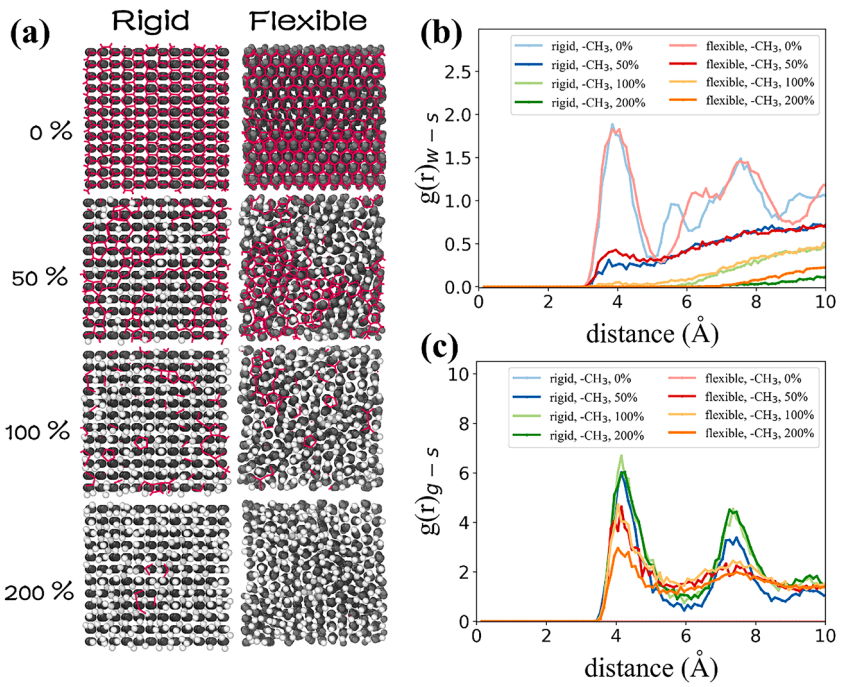

Fig. 5. Impact of surface flexibility on IML/alkyl monolayer interfacial structures. (a) 2D top view of the alkyl monolayer and interfacial components for systems with various gas concentrations. (b) Radial distribution functions (RDF) of water molecules on rigid and flexible alkyl monolayers. (c) RDF of gas molecules on rigid and flexible alkyl monolayers.

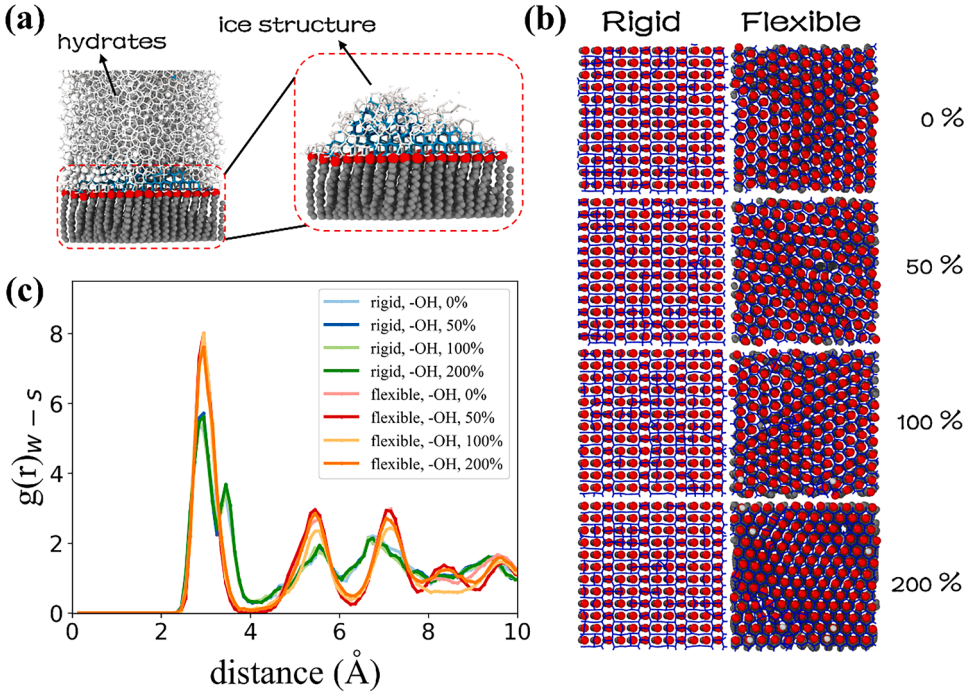

Fig. 6. Impact of surface fluctuation on IML/alcohol monolayer interfacial structures. (a) Schematic of interface water (ice) structure on alcohol monolayer. (b) Snapshots of the alcohol monolayer and interfacial components for systems with various gas concentrations (2D top view). (c) RDF of water molecules on rigid and flexible alcohol monolayer.

labeled as F (flexible) and R (rigid), respectively. The results indicate that, for systems with the same gas content, surface functional group or wettability of the substrate is the primary factor influencing adhesion strength. The presence of hydrophilic groups (-OH) on the monolayers significantly altered the fracture behavior of hydrate , transitioning it from primarily adhesive to predominantly cohesive failure. This represents a noteworthy distinction in hydrate fracture behavior compared to smooth solid surfaces [21,23]. In comparison, the contribution of surface fluctuation to adhesion strength is limited, at least on hydrophobic monolayers. This is attributed to the fact that the measured adhesion strength of the system is primarily determined by the adjacent layers along the fracture interface. The flexibility of the hydrophobic

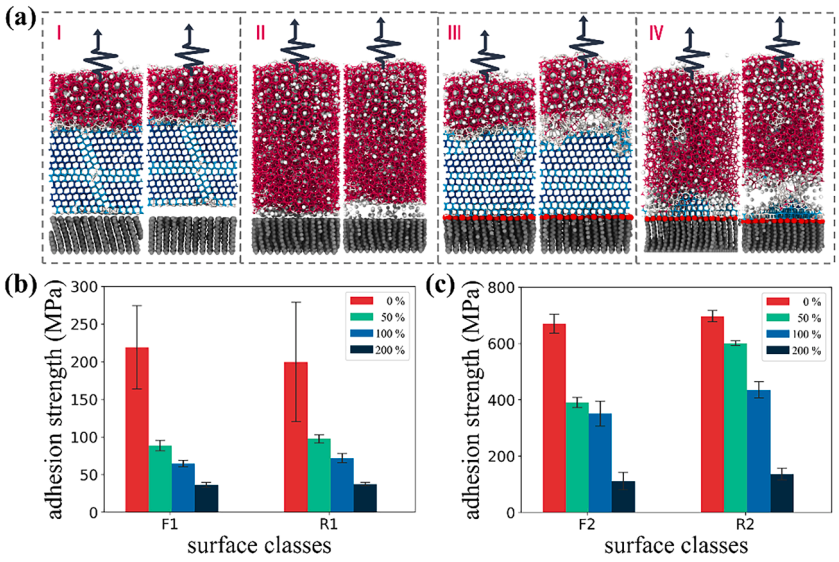

Fig. 7. Tensile testing of stable hydrate adhesion configurations with different monolayers. (a) Comparison snapshots before and after the tensile rupture of four sets of typical configurations: I. Breakage of ice on alkyl monolayer; II. Breakage of hydrates on alkyl monolayer; III. Breakage of ice on alcohol monolayer; IV. Breakage of hydrate on alcohol monolayer. (b) Adhesion strengths on flexible and rigid alkyl monolayers measured from systems containing different gas contents. (c) Adhesion strengths on flexible and rigid alcohol monolayers measured from systems containing different gas contents. In (b) and (c), "F" and "R" respectively indicate whether the data originates from the "flexible" monolayer or the "rigid" monolayer.

monolayer did not significantly alter the composition of adjacent layers.

For hydrophobic monolayers, the measured adhesion strength primarily decreases with increasing gas content in the system (Fig. 7b). This phenomenon is attributed to the gas enrichment at the hydrophobic interface, as confirmed by the component analysis of the IML interface near the monolayer (Fig. 8a), consistent with observations in previous studies of hydrate adhesion on hydrophobic solid surfaces [21,23]. Moreover, it has been experimentally confirmed that the adhesion strength of hydrates even can be reduced to zero [25] by a "gas coating" through the implementation of interfacial gas-enrichment strategy [23]. Furthermore, in systems containing hydrophobic (-CH_3) monolayers, the breaks were always adhesive failures (Fig. 7a-I, II), as the IML water structure only experiences van der Waals interactions with the substrate. It is worth noting that the larger standard error observed in adhesion strength measured in pure water systems (0 %) is due to the final solidified IML can be into ice or hydrate structures, as mentioned in Section 3.1.2 (Fig. 3d).

For hydrophilic monolayers, while the measured adhesion strength also shows a decreasing trend with increasing gas content in IML, its fracture behavior is more complex. This complexity often arises from uncertainty in the fracture location. As mentioned in Section 3.3, hydroxylated monolayers consistently lead to the generation of a dense water layer (ice structure) at the interface and repel gas molecules. The interface component analysis of IML/monolayers also confirms this phenomenon, as shown in Fig. 8b. Hydroxylated surfaces consistently adsorb water molecules from IML to form dense structures, independent of the gas content within. In this scenario, water molecules in the adjacent layer can form hydrogen bonds with the hydroxyl groups on monolayers, significantly strengthening the interface. Therefore, in systems with hydroxylated monolayers, the breaks were always cohesive failures, and there are always remnants of water structures on the monolayers after the fracture, as depicted in Fig. 7a-III, IV.

3.5. *Relationship between fracture locations and corresponding interface strength*

To further investigate the influence of surface property, gas concentration, and fracture locations on the measured adhesion strength, this section categorizes six representative structures from the fracture test results, as shown in Fig. 9. While Fig. 10 displays the force-time curves of these six typical configurations during the tensile tests. Since all systems have the same cross-sectional area (the area of monolayers),

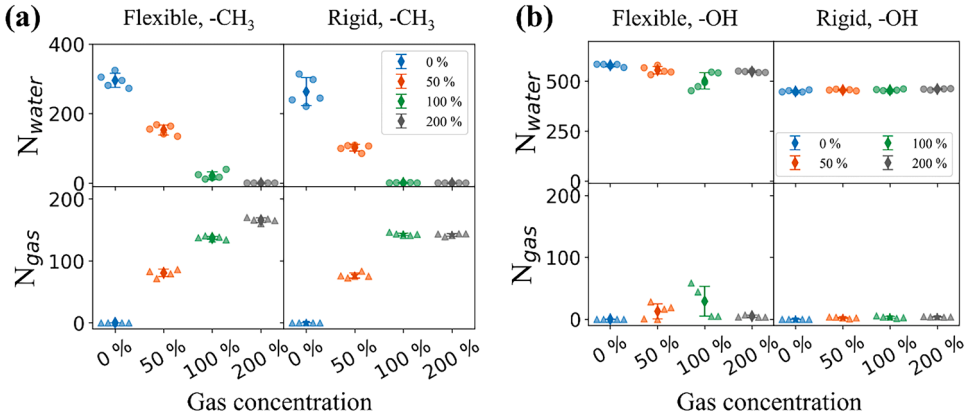

Fig. 8. Interfacial component analysis. The number of water and gas molecules at the IML/monolayer interface in systems containing different gas content: (a) on the alkyl monolayers, and (b) on the alcohol monolayers. The thickness of interfacial layer is referenced to the position of the first peak in the corresponding RDF.

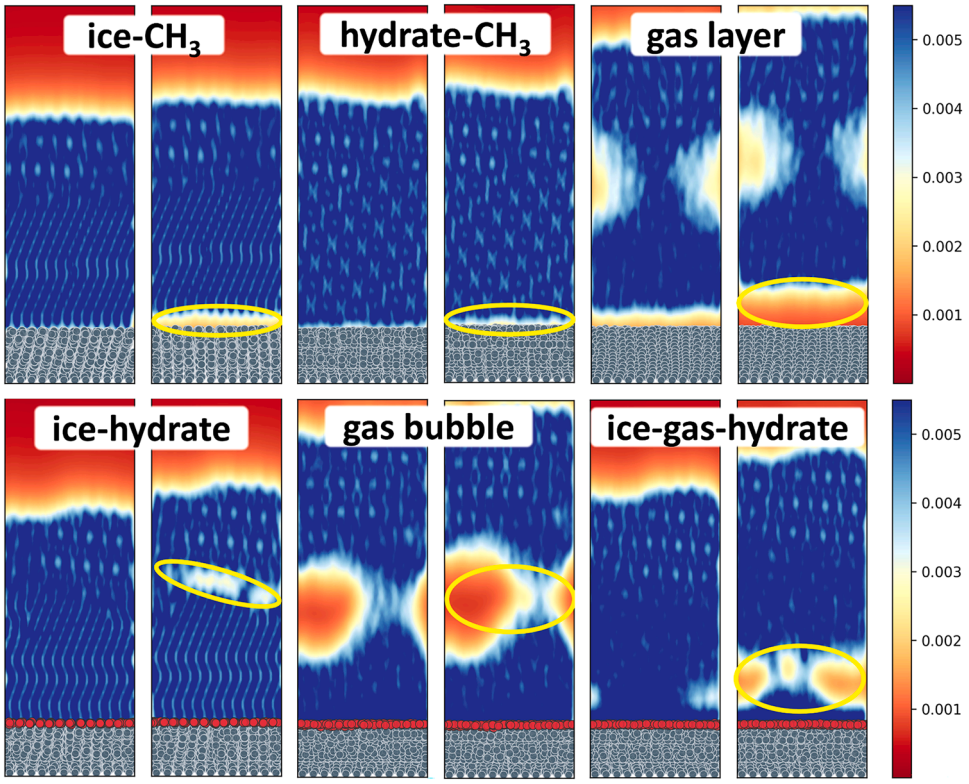

Fig. 9. Two-dimensional density projections of water molecules before and after the fracture of six representative solidification configurations. Yellow circles mark the fracture positions, and the text within white boxes names these fracture interfaces.

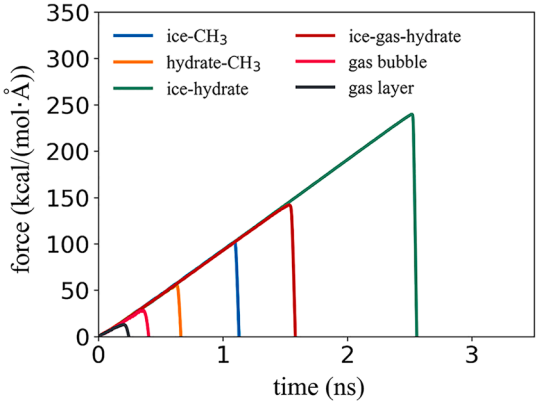

Fig. 10. Spring force recorded over time during stretching corresponds to six representative solidification configurations. The involvement of hydrogen bonds significantly enhances the fracture interface.

directly comparing the force is equivalent to comparing adhesion strength.

For hydrophobic monolayers, all fracture locations occur at the IML/monolayer interface. In these cases, the stable configuration after IML solidification determines the measured adhesion strength. The maximum spring force experienced during the fracture test indicates that the ice-CH_3 interface > hydrate-CH_3 interface > gas layer interface. In other words, ice exhibits the highest adhesion strength, nearly twice that of pure hydrate lattice, while the gas enrichment at the interface consistently weakens the interface, aligning with observations of solid surface cases [21,23].

For systems containing hydroxylated monolayers, fractures can occur at the interfaces of hydrate-ice, gas bubbles, and ice-gas-hydrate three-phase boundaries during tensile testing. Hydrogen bonds significantly enhance the fracture surface, constituting the primary reason for the higher adhesion strength observed in these systems. Additionally, the presence and size of internal gas bubbles also significantly affect interface strength. A larger proportion of gas on the fracture surface implies fewer hydrogen bonds, leading to the following sequence of interface strength: ice-hydrate interface > ice-gas-hydrate interface > gas bubble interface.

4. Conclusions

In this study, the complex interaction of factors influencing the adhesion strength of gas hydrates to soft material represented by organic monolayers is unveiled. A crucial role is played by surface functional groups in controlling adhesion strength. Hydrate adhesion on hydrophobic monolayers is solely affected by van der Waals interactions with interfacial water molecules and can be fatally weakened by forming “gas coating”. Hydrate adhesion is significantly enhanced by hydrophilic functional groups. The hydrophilic functional groups, such as hydroxyl (-OH) groups, play a prominent role through hydrogen bonding interactions. The involvement of hydrogen bonds results in a shift from adhesive failure to cohesive failure, concurrently significantly increasing adhesion strength. This enhancing adhesion mechanism is a significant departure from smooth hydrophilic solid surfaces. Additionally, multiple potential fracture locations are identified during the tensile testing of the stable adhesion structures, with the highest adhesion strength observed at the ice/hydrate interface. This discovery highlights the importance of considering potential fracture locations when designing anti-hydrate surfaces. The limited impact of the flexibility of monolayers is observed, especially in the case of hydrophobic ones. This observation may also be attributed to the tightly packed nature of the monolayer. These novel insights contribute to a more comprehensive understanding of gas hydrate adhesion on surfaces and will lead to the design and development of more effective anti-hydrate surface materials.

CRediT authorship contribution statement

Rui Ma: Conceptualization, Writing – original draft. **Senbo Xiao:** Validation, Software. **Yuanhao Chang:** Methodology. **Jianying He:** Writing – review & editing. **Zhiliang Zhang:** Writing – review & editing, Supervision.

Declaration of competing interest

The authors declare that they have no known competing financial interests or personal relationships that could have appeared to influence the work reported in this paper.

Data availability

No data was used for the research described in the article.

Acknowledgments

We are grateful for the support of the Research Council of Norway through the D'andra project (Project No. 302348). The supercomputer CPU hours were provided by the Norwegian Metacenter for Computational Science (Grant No. NN9110K, NN9391K, and NN8084K).

References

[1] C.A. Koh, A.K. Sum, E.D. Sloan, Gas hydrates: unlocking the energy from icy cages, J. Appl. Phys. 106 (2009) 9.
[2] E.D. Sloan, Natural Gas Hydrates in Flow Assurance, Gulf Professional Publishing, 2010.
[3] M. Akhfash, Z.M. Aman, S.Y. Ahn, M.L. Johns, E.F. May, Gas hydrate plug formation in partially-dispersed water–oil systems, Chem. Eng. Sci. 140 (2016) 337–347.
[4] Z. Wang, J. Zhang, B. Sun, L. Chen, Y. Zhao, W. Fu, A new hydrate deposition prediction model for gas-dominated systems with free water, Chem. Eng. Sci. 163 (2017) 145–154.
[5] X. Zhang, B.R. Lee, J.H. Sa, K.J. Kinnari, K.M. Askvik, X. Li, A.K. Sum, Hydrate management in deadlegs: effect of wall temperature on hydrate deposition, Energy Fuels 32 (2018) 3254–3262.
[6] Z. Liu, Z. Liu, J. Wang, M. Yang, J. Zhao, Y. Song, Hydrate blockage observation and removal using depressurization in a fully visual flow loop, Fuel 294 (2021) 120588.
[7] Z. Liu, Y. Li, W. Wang, G. Song, Y. Ning, X. Liu, J. Zhang, Investigation into the formation, blockage and dissociation of cyclopentane hydrate in a visual flow loop, Fuel 307 (2022) 121730.
[8] H.J. Ng, D.B. Robinson, Hydrate formation in systems containing methane, ethane, propane, carbon dioxide or hydrogen sulfide in the presence of methanol, Fluid Phase Equilib. 21 (1985) 145–155.
[9] E.D. Sloan Jr, C.A. Koh, Clathrate Hydrates of Natural Gases, CRC Press, 2007.
[10] Z.T. Ward, R.A. Marriott, A.K. Sum, E.D. Sloan, C.A. Koh, Equilibrium data of gas hydrates containing methane, propane, and hydrogen sulfide, J. Chem. Eng. Data 60 (2015) 424–428.
[11] N.N. Nguyen, R.D. Berger, H.J.R. Butt, Premelting-induced agglomeration of hydrates: theoretical analysis and modeling, ACS Appl. Mater. Interfaces 12 (2020) 14599–14606.
[12] B. Shi, S. Song, Y. Chen, X. Duan, Q. Liao, S. Fu, L. Liu, J. Sui, J. Jia, H. Liu, Status of natural gas hydrate flow assurance research in China: a review, Energy Fuels 35 (2021) 3611–3658.
[13] A. Perrin, O.M. Musa, J.W. Steed, The chemistry of low dosage clathrate hydrate inhibitors, Chem. Soc. Rev. 42 (2013) 1996–2015.
[14] W. Ke, M.A. Kelland, Kinetic hydrate inhibitor studies for gas hydrate systems: a review of experimental equipment and test methods, Energy Fuels 30 (2016) 10015–10028.
[15] W. Ke, D. Chen, A short review on natural gas hydrate, kinetic hydrate inhibitors and inhibitor synergists, Chin. J. Chem. Eng. 27 (2019) 2049–2061.
[16] H.J. Noh, D. Lee, W. Go, G. Choi, Y.K. Im, J. Mahmood, Y. Seo, J.B. Baek, Fused aromatic networks as a new class of gas hydrate inhibitors, Chem. Eng. J. 433 (2022) 133691.
[17] C.B. Bavoh, O. Nashed, A.N. Rehman, N.A.A.B. Othaman, B. Lal, K.M. Sabil, Ionic liquids as gas hydrate thermodynamic inhibitors, Ind. Eng. Chem. Res. 60 (2021) 15835–15873.
[18] Y. Gong, R.I. Mendgaziev, W. Hu, Y. Li, Z. Li, A.S. Stoporev, A.Y. Manakov, V. A. Vinokurov, T. Li, A.P. Semenov, Urea as a green thermodynamic inhibitor of sII gas hydrates, Chem. Eng. J. 429 (2022) 132386.
[19] J. Zhao, C. Lang, J. Chu, L. Yang, L. Zhang, Flow assurance of hydrate risk in natural gas/oil transportation: state-of-the-art and future challenges, J. Phys. Chem. C 127 (2023) 13439–13450.
[20] S. Dong, M. Li, C. Liu, J. Zhang, G. Chen, Bio-inspired superhydrophobic coating with low hydrate adhesion for hydrate mitigation, J. Bionic. Eng. 17 (2020) 1019–1028.
[21] R. Ma, F. Wang, Y. Chang, S. Xiao, N.J. English, J. He, Z. Zhang, Unraveling adhesion strength between gas hydrate and solid surfaces, Langmuir 37 (2021) 13873–13881.
[22] F. Wang, R. Ma, S. Xiao, N.J. English, J. He, Z. Zhang, Anti-gas hydrate surfaces: perspectives, progress and prospects, J. Mater. Chem. A (2022).
[23] R. Ma, S. Xiao, Y. Chang, Y. Fu, J. He, Z. Zhang, An interfacial gas-enrichment strategy for mitigating hydrate adhesion and blockage, Chem. Eng. J. 453 (2023) 139918.
[24] A. Mund, A.K. Nayse, A. Das, Design of a liquid impregnated surface with a stable lubricant layer in a mixed water/oil environment for low hydrate adhesion, Langmuir (2023).
[25] W. Zhang, S. Fan, G. Li, Y. Wang, X. Lang, Multifunctional amphiphobic coating toward ultralow interfacial adhesion of hydrates, Langmuir 39 (2023) 4082–4090.
[26] Z. He, E.T. Vågenes, C. Delabahan, J. He, Z. Zhang, Room temperature characteristics of polymer-based low ice adhesion surfaces, Sci. Rep. 7 (2017) 1–7.
[27] Z. He, S. Xiao, H. Gao, J. He, Z. Zhang, Multiscale crack initiator promoted super-low ice adhesion surfaces, Soft Matter 13 (2017) 6562–6568.
[28] Y. Zhuo, V. Håkonsen, Z. He, S. Xiao, J. He, Z. Zhang, Enhancing the mechanical durability of icephobic surfaces by introducing autonomous self-healing function, ACS Appl. Mater. Interfaces 10 (2018) 11972–11978.
[29] F. Wang, S. Xiao, Y. Zhuo, W. Ding, J. He, Z. Zhang, Liquid layer generators for excellent icephobicity at extremely low temperatures, Mater. Horiz. 6 (2019) 2063–2072.
[30] T. Li, P.F. Ibáñez-Ibáñez, V. Håkonsen, J. Wu, K. Xu, Y. Zhuo, S. Luo, J. He, Z. Zhang, Self-deicing electrolyte hydrogel surfaces with pa-level ice adhesion and durable antifreezing/antifrost performance, ACS Appl. Mater. Interfaces 12 (2020) 35572–35578.
[31] F. Wang, S. Xiao, J. He, F. Ning, R. Ma, J. He, Z. Zhang, Onion inspired hydrate-phobic surfaces, Chem. Eng. J. 437 (2022) 135274.
[32] K. Golovin, A. Dhyani, M. Thouless, A. Tuteja, Low–interfacial toughness materials for effective large-scale deicing, Science 364 (2019) 371–375 (1979).
[33] Z. He, Y. Zhuo, F. Wang, J. He, Z. Zhang, Design and preparation of icephobic PDMS-based coatings by introducing an aqueous lubricating layer and macro-crack initiators at the ice-substrate interface, Prog. Org. Coat. 147 (2020) 105737.
[34] Z. He, Y. Zhuo, Z. Zhang, J. He, Design of icephobic surfaces by lowering ice adhesion strength: a mini review, Coatings 11 (2021) 1343.
[35] M.J. Wood, G. Brock, P. Servio, A.M. Kietzig, Leveraging solidification dynamics to design robust ice-shedding surfaces, ACS Appl. Mater. Interfaces 14 (2022) 38379–38387.
[36] X. Jiang, Y. Lin, X. Xuan, Y. Zhuo, J. Wu, J. He, X. Du, Z. Zhang, T. Li, Stiffening surface lowers ice adhesion strength by stress concentration sites, Colloids Surf. A Physicochem. Eng. Asp. 666 (2023) 131334.
[37] M.I. Jamil, X. Zhan, F. Chen, D. Cheng, Q. Zhang, Durable and scalable candle soot icephobic coating with nucleation and fracture mechanism, ACS Appl. Mater. Interfaces 11 (2019) 31532–31542.
[38] R. Pan, H. Zhang, M. Zhong, Triple-scale superhydrophobic surface with excellent anti-icing and icephobic performance via ultrafast laser hybrid fabrication, ACS Appl. Mater. Interfaces 13 (2020) 1743–1753.
[39] M. Huré, P. Olivier, J. Garcia, Effect of Cassie-Baxter versus Wenzel states on ice adhesion: a fracture toughness approach, Cold Reg. Sci. Technol. 194 (2022) 103440.
[40] Z. He, Y. Zhuo, F. Wang, J. He, Z. Zhang, Understanding the role of hollow sub-surface structures in reducing ice adhesion strength, Soft Matter 15 (2019) 2905–2910.
[41] M. Grizen, M.K. Tiwari, Icephobic surfaces: features and challenges, Ice Adhesion: mechanism, Meas. Mitig. (2020) 417–466.
[42] Y. Zhuo, J. Chen, S. Xiao, T. Li, F. Wang, J. He, Z. Zhang, Gels as emerging anti-icing materials: a mini review, Mater. Horiz. 8 (2021) 3266–3280.
[43] Y. Qiu, N. Odendahl, A. Hudait, R. Mason, A.K. Bertram, F. Paesani, P.J. DeMott, V. Molinero, Ice nucleation efficiency of hydroxylated organic surfaces is controlled by their structural fluctuations and mismatch to ice, J. Am. Chem. Soc. 139 (2017) 3052–3064.
[44] C. Chen, Y. Zhang, J. Sun, Y. Liu, Y. Qin, Z. Ling, W. Liu, W. Li, The roles of functional groups of antifreeze protein in inhibition of hydrate growth, Fuel 327 (2022) 125060.
[45] S.M. Marks, A.J. Patel, Antifreeze protein hydration waters: unstructured unless bound to ice, Proc. Natl. Acad. Sci. 115 (2018) 8244–8246.
[46] L. Seeley, G. Seidler, Preactivation in the nucleation of ice by Langmuir films of aliphatic alcohols, J. Chem. Phys. 114 (2001) 10464–10470.
[47] D.A. Knopf, S.M. Forrester, Freezing of water and aqueous NaCl droplets coated by organic monolayers as a function of surfactant properties and water activity, J. Phys. Chem. A 115 (2011) 5579–5591.
[48] R. Popovitz-Biro, J. Wang, J. Majewski, E. Shavit, L. Leiserowitz, M. Lahav, Induced freezing of supercooled water into ice by self-assembled crystalline monolayers of amphiphilic alcohols at the air-water interface, J. Am. Chem. Soc. 116 (1994) 1179–1191.
[49] F.H. Stillinger, T.A. Weber, Computer simulation of local order in condensed phases of silicon, Phys. Rev. B 31 (1985) 5262.
[50] V. Molinero, E.B. Moore, Water modeled as an intermediate element between carbon and silicon, J. Phys. Chem. B 113 (2009) 4008–4016.
[51] L.C. Jacobson, W. Hujo, V. Molinero, Nucleation pathways of clathrate hydrates: effect of guest size and solubility, J. Phys. Chem. B 114 (2010) 13796–13807.

[52] L.C. Jacobson, V. Molinero, A methane− water model for coarse-grained simulations of solutions and clathrate hydrates, J. Phys. Chem. B 114 (2010) 7302–7311.
[53] B.C. Knott, V. Molinero, M.F. Doherty, B. Peters, Homogeneous nucleation of methane hydrates: unrealistic under realistic conditions, J. Am. Chem. Soc. 134 (2012) 19544–19547.
[54] A.H. Nguyen, L.C. Jacobson, V. Molinero, Structure of the clathrate/solution interface and mechanism of cross-nucleation of clathrate hydrates, J. Phys. Chem. C 116 (2012) 19828–19838.
[55] L. Lupi, A. Hudait, V. Molinero, Heterogeneous nucleation of ice on carbon surfaces, J. Am. Chem. Soc. 136 (2014) 3156–3164.
[56] A.H. Nguyen, M.A. Koc, T.D. Shepherd, V. Molinero, Structure of the ice–clathrate interface, J. Phys. Chem. C 119 (2015) 4104–4117.
[57] W.L. Jorgensen, J.D. Madura, C.J. Swenson, Optimized intermolecular potential functions for liquid hydrocarbons, J. Am. Chem. Soc. 106 (1984) 6638–6646.
[58] Y. Qiu, V. Molinero, Morphology of liquid–liquid phase separated aerosols, J. Am. Chem. Soc. 137 (2015) 10642–10651.
[59] S. Plimpton, Fast parallel algorithms for short-range molecular dynamics, J. Comput. Phys. 117 (1995) 1–19.
[60] W.G. Hoover, Canonical dynamics: equilibrium phase-space distributions, Phys. Rev. A 31 (1985) 1695.
[61] W.G. Hoover, Constant-pressure equations of motion, Phys. Rev. A 34 (1986) 2499.
[62] A. Stukowski, Visualization and analysis of atomistic simulation data with OVITO–the open visualization tool, Model. Simul. Mat. Sci. Eng. 18 (2009) 015012.
[63] S. Xiao, J. He, Z. Zhang, Nanoscale deicing by molecular dynamics simulation, Nanoscale 8 (2016) 14625–14632.
[64] Z.M. Aman, W.J. Leith, G.A. Grasso, E.D. Sloan, A.K. Sum, C.A. Koh, Adhesion force between cyclopentane hydrate and mineral surfaces, Langmuir 29 (2013) 15551–15557.
[65] N.N. Nguyen, R.D. Berger, M. Kappl, H.J.R. Butt, Clathrate adhesion induced by quasi-liquid layer, J. Phys. Chem. C 125 (2021) 21293–21300.
[66] A.H. Nguyen, V. Molinero, Identification of clathrate hydrates, hexagonal ice, cubic ice, and liquid water in simulations: the CHILL+ algorithm, J. Phys. Chem. B 119 (2015) 9369–9376.
[67] L. Li, J. Zhong, Y. Yan, J. Zhang, X.C. Zeng, Unraveling nucleation pathway in methane clathrate formation, Proc. Natl. Acad. Sci. (2020) 117.
[68] D. Kainai, D. Bai, Effect of cage occupancy on stability and decomposition of methane hydrate, J. Phys. Chem. B 126 (2022) 492–502.
[69] Z. He, P. Linga, J. Jiang, CH_4 hydrate formation between silica and graphite surfaces: insights from microsecond molecular dynamics simulations, Langmuir ACS J. Surf. Colloids (2017) 7b02711, acs.langmuir.
[70] B. Fang, F. Ning, W. Ou, D. Wang, Z. Zhang, Y. Yu, H. Lu, J. Wu, T.J. Vlugt, The dynamic behavior of gas hydrate dissociation by heating in tight sandy reservoirs: a molecular dynamics simulation study, Fuel 258 (2019) 116106.